Parametric processes in quasi-phasematching gratings with random duty cycle errors

C. R. Phillips,* J. S. Pelc, and M. M. Fejer

E. L. Ginzton Laboratory, Stanford University, 348 Via Palou, Stanford, California 94305, USA
**Corresponding author: cphillips@phys.ethz.ch*

Received December 5, 2012; accepted February 13, 2013;
posted February 19, 2013 (Doc. ID 181205); published March 22, 2013

Random duty cycle (RDC) errors in quasi-phase-matching (QPM) gratings lead to a pedestal in the spatial-frequency spectrum that increases the conversion efficiency for nominally phase-mismatched processes. Here, we determine the statistical properties of the Fourier spectrum of the QPM grating in the presence of RDC errors. We illustrate these properties with examples corresponding to periodic gratings with parameters typical for continuous-wave interactions, and chirped gratings with parameters typical for devices involving broad optical bandwidths. We show how several applications are sensitive to RDC errors by calculating the conversion efficiency of relevant nonlinear-optical processes. Last, we propose a method to efficiently incorporate RDC errors into coupled-wave models of nonlinear-optical interactions while still retaining only a small number of QPM grating orders.

OCIS codes: 190.4410, 190.4360, 230.7405, 190.4970.

1. INTRODUCTION

In a wide variety of experiments using quasi-phase-matching (QPM) gratings, multiple nonlinear conversion processes can occur simultaneously, whether by design [1–8] or as a natural (and possibly parasitic) consequence of the desired device configuration [9–27]. Such parasitic processes can play an important role in many contexts, including frequency conversion of quantum states of light [8–13], optical parametric oscillators (OPOs) [14–20], optical parametric amplification (OPA) [21–23], and QPM supercontinuum generation [24–27]. The types of parasitic processes considered in this paper are nominally phase-mismatched nonlinear interactions, which, in QPM gratings with random variations in the duty cycle, can occur with efficiencies significantly higher than would be expected given an ideal QPM grating and a large phase mismatch [28,29].

In periodically or aperiodically poled lithium niobate (PPLN and APPLN, respectively), these nonidealities typically correspond to the ferroelectric domain boundaries not lying at their ideal (designed) positions [29,30]. When the errors in the domain boundary positions have stationary statistics (as is typically the case for lithographically defined QPM patterns), and in particular when these errors are independent and identically distributed (IID), they are termed random duty cycle (RDC) errors [29]. While these RDC errors usually have only a weak effect on the conversion efficiency near the QPM peak, they give rise to a "pedestal" in the spatial-frequency spectrum of the grating. Away from the phase-matching peak of the ideal structure, this QPM noise pedestal is relatively flat statistically (i.e., after averaging over an ensemble of imperfect QPM gratings), unlike the Fourier spectrum of the ideal grating (which, for example, has approximately a sinc^2 form for a periodic grating). This pedestal can lead to an increase in the conversion efficiency of parasitic, nominally phase-mismatched processes compared to that expected in a perfect grating. It is therefore important to model RDC errors so that experiments can be designed that are not excessively sensitive to their effects.

In this paper, we analyze RDC errors in detail, and consider several applications where they can play a significant role. In Section 2, we first develop a general formalism for describing the QPM gratings with RDC errors, including those with arbitrary nominal duty cycle and chirp profiles. In Subsections 2.B and 2.D, we derive the statistical properties of the QPM noise pedestal itself. Our treatment readily yields results for pulsed interactions and also for backward-generated waves: these cases are discussed in Subsections 2.C and 2.E, respectively. In Section 3, we discuss the QPM noise pedestal for the cases of periodic and linearly chirped gratings. The results for these two cases will be relevant to a large fraction of QPM gratings used in practical devices.

In Section 4 we investigate a number of applications where RDC errors can play a significant (and possibly unexpected) role. We consider the following applications: dark count rates in quantum-state frequency translation, two-photon absorption (TPA) in high power optical parametric chirped pulse amplification (OPCPA), nonlinear losses in OPOs, cascaded processes in OPOs, and supercontinuum generation. This list is not intended to be exhaustive, but is representative of the importance of RDC-related effects and of how these effects can be evaluated in various different practical contexts. To analyze some of these applications, we extend the formalism of Section 2 to account for more complicated interactions, while maintaining the same overall statistical approach. For highly nonlinear interactions, however, a purely analytical approach is usually insufficient, particularly when ultrashort pulses are involved. Therefore, we also discuss in Appendix A how RDC errors could be incorporated into existing general numerical modeling tools used to simulate QPM interactions.

2. QPM GRATINGS WITH RDC ERRORS

In this section, we calculate the ensemble-averaged statistical properties of the spatial-frequency pedestal that arises due to RDC errors. We consider a three-wave difference-frequency generation (DFG) process involving monochromatic plane waves with negligible signal gain and pump depletion. Our results are directly applicable to second-harmonic generation (SHG) and sum-frequency generation (SFG), provided that depletion of the input waves can be neglected.

A. Transfer Function

Under the above assumptions, the generated idler is given by a transfer function that is related to the spatial Fourier transform (FT) of the QPM grating [31]. In this subsection, we derive this transfer function and express it in a form suitable for subsequent statistical analysis. The propagation equation for the idler envelope is given by [32]

$$\frac{dA_i}{dz} = -i\frac{\omega_i d(z)}{n_i c} A_s^* A_p e^{-i\Delta k z}, \tag{1}$$

where subscripts (i, s, p) correspond to the idler, signal, and pump, respectively. ω_j is the carrier frequency of wave j, and n_j is the refractive index evaluated at ω_j. The envelopes A_j are defined in relation to the electric field as $E = (1/2)\sum_j A_j \exp[i(\omega_j t - k_j z)] + \text{c.c.}$ (complex conjugate), where summation is performed over $j = i,\ s,\ p$ and $k_j = \omega_j n_j / c$. The phase mismatch is defined as $\Delta k = k_p - k_s - k_i$, and $d(z) = \pm d_0$ is the value of the relevant second-order nonlinear coefficient based on the $\chi^{(2)}$ tensor and the polarization directions of the interacting fields, and is inverted periodically or aperiodically in the QPM grating.

The idler field A_i can be written in a form normalized to the value it would take at the output of an ideal periodic grating, with no RDC errors, satisfying first-order QPM (for which the domain size would be given by $\Lambda_D = \pi/\Delta k$):

$$A_i = -i\frac{2L}{\pi}\frac{\omega_i d_0}{n_i c} A_s^* A_p a_i, \tag{2}$$

where a_i is the normalized idler field and L is the length of the QPM grating. With this definition, Eq. (1) can be written as

$$\frac{da_i}{dz} = \frac{\pi}{2L}\frac{d(z)}{d_0} e^{-i\Delta k z} \equiv g(z) e^{-i\Delta k z}, \tag{3}$$

where the normalized grating profile $g(z)$ is implicitly defined in Eq. (3), and $g(z) = 0$ for $z < 0$ and $z > L$. By integrating Eq. (3), it can be seen that the normalized idler output $a_i(L)$ is the spatial FT of $g(z)$, $\tilde{g}(k)$, evaluated at spatial frequency $k = \Delta k$. We define the FT of a function $f(x)$ as $\tilde{f}(k) \equiv \mathcal{F}[f(x)](k) = \int f(x) e^{-ikx} dx$, with tilde denoting a quantity expressed in the frequency domain. The square magnitude of $\tilde{g}$ gives the idler intensity relative to the "maximum" intensity achievable in a QPM grating of the same length, assuming that the pump and signal [or first harmonic (FH) in the case of SHG] are undepleted. By writing $g(z)$ as a sum of individual domains, $\tilde{g}(k)$ can be written as

$$\begin{aligned}\tilde{g}_{\mathbf{z}}(k) &= i\frac{\pi}{2kL}\sum_{n=1}^{N}(-1)^n\left(e^{-ik\mathbf{z}[n]} - e^{-ik\mathbf{z}[n-1]}\right)\\ &= i\frac{\pi}{kL}\left[\frac{e^{-ik\mathbf{z}[0]} + (-1)^N e^{-ik\mathbf{z}[N]}}{2} + \sum_{n=1}^{N-1}(-1)^n e^{-ik\mathbf{z}[n]}\right],\end{aligned} \tag{4}$$

where $\mathbf{z}$ is a vector which specifies the domain boundary positions. The notation $\tilde{g}_{\mathbf{z}}$ is used to indicate the domain boundary vector $\mathbf{z}$ being considered. We refer to $\tilde{g}_{\mathbf{z}}(k)$ as the normalized transfer function.

Next, we approximate the contributions from the first and last QPM domains (those related to the positions $\mathbf{z}[0]$ and $\mathbf{z}[N]$), in order to write $\tilde{g}_{\mathbf{z}}(k)$ in a simpler form as a summation of complex exponentials. The resulting (approximate) normalized transfer function is given by

$$\tilde{g}_{\mathbf{z}}(k) \approx i\frac{\pi}{kL}\sum_{n=1}^{N}(-1)^n e^{-ik\mathbf{z}[n]}. \tag{5}$$

Comparing Eqs. (4) and (5), we see that the approximation is perfect for an ideal grating satisfying first-order QPM, and in general its error is comparable to the contribution from a single domain.

We denote the ideal vector of domain boundary positions (those obtained in the absence of any RDC errors) as $\mathbf{z}_0$. In an ideal periodic grating, $\mathbf{z}_0[n] = n\Lambda_D$ for domain length Λ_D. For a phase-matched interaction in such an ideal periodic grating, $k = \Delta k = \pi/\Lambda_D$, in which case the summand in Eq. (5) is simply unity for each term, and so $|\tilde{g}_{\mathbf{z}_0}(\pi/\Lambda_D)| = 1$, consistent with the expected result. We assume that the components of $\mathbf{z}_0[n]$ are fixed by the nominal grating design, and that the deviations $(\mathbf{z}[n] - \mathbf{z}_0[n])$ of the domain boundaries from their ideal positions are IID. Note also that, in a real structure, the position and length of the first and last QPM domains will depend on the crystal polishing process; we neglect these and similar issues here.

B. Ensemble-Averaged Noise Pedestal and Efficiency Reduction

Following [29], we assume IID errors in the domain boundary positions. We assume a normal distribution for each of these positions with mean $\mathbf{z}_0[n]$ and variance σ_z^2, i.e., $\mathbf{z}[n] \sim \mathcal{N}(\mathbf{z}_0[n], \sigma_z^2)$. The variance in the length $l_n = \mathbf{z}[n] - \mathbf{z}[n-1]$ of each domain, σ_l^2, is related to the variance of the domain boundary positions, σ_z^2, by $\sigma_l^2 = 2\sigma_z^2$. A schematic of such RDC errors is illustrated in Fig. 1. As described in Section 1, RDC errors are typically associated with lithographically defined QPM patterns: the lithographic pattern ensures long-range order of the grating (and hence prevents period errors [29]), but any local fluctuations can lead to perturbations in the positions of the domain boundaries. After fabrication, the domains are fixed for any given grating;

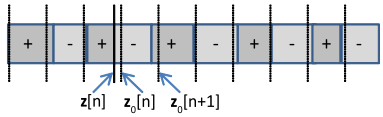

Fig. 1. (Color online) Schematic of a QPM grating with RDC errors. Vertical dashed lines indicate the ideal, equally spaced domain boundary positions. Elements of the domain boundary vectors $\mathbf{z}$ (random) and $\mathbf{z}_0$ (ideal) are indicated.

therefore, in any particular experiment, a single vector $\mathbf{z}$ applies. However, since the errors are random from one grating to the next, it is useful to calculate the expected behavior of an ensemble of devices with identically distributed errors.

As shown in [29], the ensemble-averaged mean of the normalized transfer function is given by

$$\langle \tilde{g}_{\mathbf{z}}(k) \rangle = e^{-k^2\sigma_z^2/2} \tilde{g}_{\mathbf{z}_0}(k), \tag{6}$$

where the ensemble averaging is performed over random vectors $\mathbf{z}$, and the relation

$$\langle e^{ikz} \rangle = e^{-k^2\sigma_z^2/2} e^{ik\langle z \rangle} \tag{7}$$

for scalar z has been used in each term of the sum. From Eq. (6), the expected value of the transfer function is reduced compared to that of the ideal transfer function. For example, the phase-matched DFG conversion efficiency averaged over many different QPM gratings with RDC errors, given by $\langle |\tilde{g}_{\mathbf{z}}(\Delta k)|^2 \rangle$ for DFG phase mismatch Δk, would in this case be reduced by a factor $\exp(-\Delta k^2 \sigma_z^2)$ compared to first-order QPM in an ideal grating.

In addition to reducing the peak conversion efficiency, RDC errors give rise to additional spatial-frequency components far from nominal phase matching. To see this behavior we look at the ensemble-averaged value of $|\tilde{g}_{\mathbf{z}}(k)|^2$, which, with Eq. (5), is given by

$$\begin{aligned} \langle |\tilde{g}_{\mathbf{z}}(k)|^2 \rangle &= \left(\frac{\pi}{kL}\right)^2 \left\langle \sum_{m=1}^{N} \sum_{n=1}^{N} (-1)^{n-m} e^{-ik(\mathbf{z}[n]-\mathbf{z}[m])} \right\rangle \\ &= \left(\frac{\pi}{kL}\right)^2 \Bigg[N(1 - e^{-k^2\sigma_z^2}) \\ &\quad + e^{-k^2\sigma_z^2} \sum_{n=1}^{N} \sum_{m=1}^{N} (-1)^{n-m} e^{-ik(\mathbf{z}_0[n]-\mathbf{z}_0[m])} \Bigg], \end{aligned} \tag{8}$$

where the second relation can be found by separating the first relation into terms in the summand with $m = n$ and $m \neq n$: those with $m = n$ are independent of $\mathbf{z}[n]$ and hence do not acquire an $\exp(-(k\sigma_z)^2)$ factor. The pair of summations in the second relation yields the magnitude squared of the ideal transfer function, $\tilde{g}_{\mathbf{z}_0}$ [see Eq. (5)]. Therefore, we can write Eq. (8) in a more compact and convenient form:

$$\langle |\tilde{g}_{\mathbf{z}}(k)|^2 \rangle = e^{-k^2\sigma_z^2} |\tilde{g}_{\mathbf{z}_0}(k)|^2 + N\left(\frac{\pi}{kL}\right)^2 (1 - e^{-k^2\sigma_z^2}), \tag{9}$$

where the second term is a noise pedestal in spatial frequency that originates from the RDC errors. We will refer to this pedestal as the QPM noise pedestal. The factor N associated with this pedestal is accurate provided that there are enough domains N that terms $O(1)$, which are missing in Eq. (5) due to the approximations made on the edge terms, can be neglected. For very thin crystals with small N, these edge terms would not be negligible.

For periodic QPM gratings with a 50% duty cycle, there is a particularly simple analytical form for the ideal transfer function when the edge terms are included. Assuming that $\mathbf{z}[n] = n\Lambda_D$ and defining $\Delta k_1 = k - \pi/\Lambda_D$, it can be shown that [33]

$$|\tilde{g}_{\mathbf{z}_0}(k)|^2 = \left[\frac{\pi}{2} \operatorname{sinc}\left(\frac{k\Lambda_D}{2}\right)\right]^2 \left[\frac{\sin(N\Delta k_1 \Lambda_D/2)}{N \sin(\Delta k_1 \Lambda_D/2)}\right]^2. \tag{10}$$

The first factor in square brackets represents the reduced Fourier amplitudes in higher orders of the QPM grating relative to the first-order. The second factor is a "comb of sinc's," which gives rise to tuning curves at each odd order of QPM. Equation (10) is analogous to the intensity function for multislit diffraction [33].

In more general cases involving aperiodic QPM designs, simple analytical solutions to $\tilde{g}_{\mathbf{z}_0}$ analogous to Eq. (10) are often unavailable. For such cases, the Fourier spectrum can be written as a sum over the harmonics of the fundamental spatial frequency of the grating. For an aperiodic grating that varies slowly enough with z that a sensible local spatial frequency can be defined, it is convenient to write this sum in terms of a local phase function $\phi(z)$ and duty cycle $D(z)$ as

$$\begin{aligned} \frac{d(z)}{d_0} &\equiv \operatorname{sgn}[\cos(\phi(z)) - \cos(\pi D(z))] \\ &\equiv (2D(z) - 1) + \sum_{\substack{m=-\infty \\ m\neq 0}}^{\infty} \frac{2\sin(\pi m D(z))}{\pi m} \exp(im\phi(z)). \end{aligned} \tag{11}$$

The first relation corresponds to the assumption that $d(z)/d_0 = \pm 1$, as is the case, for example, for 180 deg domains in ferroelectrics, and the second relation is a trigonometric identity. The grating phase profile $\phi(z)$ is linear in position for periodic gratings, quadratic for linearly chirped gratings, and so on. When simple closed-form expressions for the summation in Eq. (5) are not available, one can use Eq. (11) to re-express the right-hand side of Eq. (3) as a sum of the contributions from the relevant QPM orders, whose individual Fourier spectra may have simple closed-form solutions. For example, these individual Fourier spectra correspond to sinc functions for periodic gratings, and to error functions for linearly chirped gratings [31,34].

Writing $g_{\mathbf{z}}(z)$ from Eq. (3) using Eq. (11) and taking the FT results in a series of terms for the normalized transfer function. These terms are given by

$$\tilde{g}_{\mathbf{z}}^{(m)}(k) = \frac{1}{mL} \sin(\pi m D) \int_0^L \exp[i(m\phi(z') - kz')] dz', \tag{12}$$

where a constant value of $D(z)$ has been assumed; this assumption is possible because random errors in the domain boundaries can in general be represented by $\phi(z)$. $\tilde{g}_{\mathbf{z}}(k)$ is found by summing $\tilde{g}_{\mathbf{z}}^{(m)}(k)$ over all indices $m \neq 0$, and then adding the normalized transfer function $\tilde{g}_{\mathbf{z}}^{dc}(k)$ that corresponds to the zeroth-order of the QPM grating. This term is independent of $\phi(z)$ and is given by [31]

$$\tilde{g}_{\mathbf{z}}^{(dc)}(k) = \frac{\pi}{2}(2D - 1) e^{-ikL/2} \operatorname{sinc}\left(\frac{kL}{2}\right). \tag{13}$$

Equation (9) thus provides a way to evaluate the ensemble-averaged transfer function for arbitrary grating structures.

C. Transfer Function Applied to Pulsed Interactions

The normalized transfer function $\tilde{g}_{\mathbf{z}}(k)$ can be directly applied to pulsed interactions, provided that certain conditions

relating to the phase mismatch are met. For pump, signal, and idler pulses with nonoverlapping spectra, the total electric field can be written in the frequency domain as

$$\tilde{E}(z,\omega)u(\omega) = \frac{1}{2}\sum_j \tilde{A}_j(z,\omega)\exp(-ik(\omega)z), \tag{14}$$

where $u(\omega)$ denotes the Heaviside step function, and A_j are analytic signals containing only positive Fourier components. We will always assume here that both the pump and signal propagate linearly, i.e., $\tilde{A}_j(z,\omega) = \tilde{A}_j(0,\omega)$ for $j = s$ and $j = p$; therefore, the z-arguments of A_s and A_p will be suppressed. With these envelope definitions, the evolution of each (positive) spectral component of the idler is given by [31]

$$\frac{d\tilde{A}_i(\omega)}{dz} = -i\frac{\omega d(z)}{n_i c}\int_0^\infty \tilde{A}_p(\omega+\omega')\tilde{A}_s^*(\omega')e^{-i\Delta k(\omega,\omega')z}\frac{d\omega'}{2\pi}, \tag{15}$$

where the frequency-dependent phase mismatch is given by

$$\Delta k(\omega,\omega') = k(\omega+\omega') - k(\omega) - k(\omega'). \tag{16}$$

When analyzing pulsed interactions, we denote the carrier frequencies as ω_j for wave j, and the carrier wave vectors as $k_j = k(\omega_j)$ (assuming the same polarization for each wave). Consider a case where the signal and pump have comparable group velocities, such that the temporal walk-off of the signal and pump pulses is negligible during propagation. This condition implies that $v_s \approx v_p$, where the frequency-dependent group velocity is given by $v_g^{-1} = dk/d\omega$, and $v_j = v_g(\omega_j)$. If in addition neither the signal nor the pump pulses disperse significantly [i.e., if group velocity dispersion (GVD) is negligible over the spectral bandwidth of the pulses], the general frequency-dependent phase mismatch can be approximated as [31]

$$\Delta k(\omega,\omega') \approx k_p - k_s + \frac{\omega-\omega_i}{v_p} - k(\omega), \tag{17}$$

which depends only on the driven idler frequency ω but not the intermediate frequency ω'. With this approximation, the integral in Eq. (15) can be simplified as a convolution. Furthermore, because each idler spectral component is driven by a particular phase mismatch, integration versus z yields a functional form proportional to $\tilde{g}_{\mathbf{z}}(\Delta k(\omega))$:

$$\tilde{A}_i(\omega) = -i\frac{2L}{\pi}\frac{\omega d_0}{n(\omega)c}\tilde{g}_{\mathbf{z}}(\Delta k(\omega)) \times \mathcal{F}[A_p(z=0,t)A_s(z=0,t)^*](\omega). \tag{18}$$

It is useful to calculate the idler fluence W_i corresponding to this electric field, which is given by $W_i \approx (n_i\epsilon_0 c/2)\int|A_i(t)|^2dt = (n_i\epsilon_0 c/2)\int|\tilde{A}_i(\omega)|^2d\omega/(2\pi)$. Since each spectral component of $\tilde{A}_i$ is, in this approximation, proportional to $\tilde{g}_{\mathbf{z}}(\Delta k(\omega))$, the fluence is an integral involving $\tilde{g}$ evaluated at different spatial frequencies, and, hence, these can each be ensemble averaged separately. If we assume that the dominant contribution to $\langle|\tilde{g}_{\mathbf{z}}(\Delta k(\omega))|^2\rangle$ is the QPM noise pedestal over all the idler frequencies ω of interest (i.e., that we are interested in a parasitic process rather than a nominally phase-matched one), and that variations of this pedestal are small over this same frequency interval, then, with the result for $\tilde{g}_{\mathbf{z}}$ from Eq. (9) inserted into Eq. (18), the ensemble-averaged idler fluence is given by

$$\langle W_i\rangle \approx \frac{2\epsilon_0\omega_i^2 d_0^2 L\Lambda_D}{n_i c}\frac{1-e^{-\Delta k(\omega_i)^2\sigma_z^2}}{\Delta k(\omega_i)^2\Lambda_D^2} \times \int|A_p(z=0,t)A_s(z=0,t)^*|^2dt. \tag{19}$$

The condition that the signal and pump negligibly walk off each other does not always apply, but Eq. (19) still provides a useful estimate of the importance of parasitic processes phase matched by the QPM noise pedestal. With analogous starting assumptions, similar results can be obtained for other types of interactions, such as pulsed SHG.

D. Fluctuations in the QPM Noise Pedestal

In some experimental configurations, the fluctuations in $|\tilde{g}_{\mathbf{z}}(k)|^2$ as a function of spatial frequency k, and, hence, phase matching for the corresponding optical frequency, may be important. For example, for pulsed interactions of the type discussed in Subsection 2.C, the output spectrum will fluctuate along with $\tilde{g}_{\mathbf{z}}(\Delta k(\omega))$. These fluctuations can be quantified via the variance of the spatial FT of the grating. Calculation of this variance through ensemble averaging is, as with the mean, significantly simplified by approximating the contributions of the edge terms. In this subsection, we therefore assume that N is large enough that $\tilde{g}_{\mathbf{z}}$ is well-approximated by Eq. (5).

By evaluating the second- and fourth-order moments $\langle|\tilde{g}_{\mathbf{z}}(k)|^2\rangle$ and $\langle|\tilde{g}_{\mathbf{z}}(k)|^4\rangle$, the standard deviation σ_η of the normalized transfer function can be determined. As with $\langle|\tilde{g}_{\mathbf{z}}^2|\rangle$ in Eq. (8), $\langle|\tilde{g}_{\mathbf{z}}^4|\rangle$ can be calculated by splitting the corresponding quadruple summation up into terms with different numbers of distinct indices, ensemble averaging, and rearranging the result in terms of $\tilde{g}_{\mathbf{z}_0}$. After some algebra, we find that

$$\begin{aligned}\langle|\tilde{g}_{\mathbf{z}}(k)|^4\rangle \approx{}& 2N^2\left(\frac{\pi}{kL}\right)^4\left(1-e^{-(k\sigma_z)^2}\right)^2 \\ &+ 4N\left(\frac{\pi}{kL}\right)^2(1-e^{-(k\sigma_z)^2})e^{-(k\sigma_z)^2}|\tilde{g}_{\mathbf{z}_0}(k)|^2 \\ &+ e^{-2(k\sigma_z)^2}|\tilde{g}_{\mathbf{z}_0}(k)|^4.\end{aligned} \tag{20}$$

If we keep only the N^2 noise-pedestal term in this equation, then the standard deviation σ_η can be approximated according to

$$\sigma_\eta \approx N\left(\frac{\pi}{kL}\right)^2(1-e^{-k^2\sigma_z^2}). \tag{21}$$

This approximation applies for large N and values of k for which the ideal transfer function $|\tilde{g}_{\mathbf{z}_0}(k)|^2$ is negligible. We note that the standard deviation in Eq. (21) is the same as the mean $\langle|\tilde{g}_{\mathbf{z}}|^2\rangle$, as would be expected for a random walk process for the generated idler field. The magnitude of the spatial Fourier spectrum of a particular grating with RDC errors is thus with high probability within a few times the ensemble-averaged mean.

In addition to the variance, it may be important to know how rapidly the spectrum of a particular QPM grating varies with its spatial frequency. Since the rate of change in spatial frequency is related to the real-space bandwidth of the

structure (i.e., the grating length L), changes to the spatial-frequency spectrum occur over a characteristic $k \sim 2\pi/L$ scale.

E. Generation of Backward Waves

The presence of RDC errors can enhance the generation of backward waves as well as the forward waves we have considered so far. One way to approach this problem is with a transfer matrix formalism [35], in which backward waves are generated as a consequence of the nonuniformities in the nonlinear susceptibility, in particular due to the (a) periodic inversions of $d(z)$. A more straightforward approach, which is appropriate if the linear susceptibility is uniform (as is typically the case in QPM media), is to solve the evolution equation for backward wave components. For monochromatic and plane-wave idler components propagating in either the same or the opposite direction to the collinear pump and signal waves, evolution through the QPM grating is governed by the equations

$$\frac{dA_i^{(\pm)}}{dz} = \mp i \frac{\omega_i d(z)}{n_i c} A_s^* A_p e^{-i\Delta k_\pm z}, \tag{22}$$

where $\Delta k_\pm = k_p - k_s \mp k_i$. $A_i^{(\pm)}$ denotes the forward (+) and backward (−) components of the idler wave. Equation (22), which is a more general version of Eq. (1), can be integrated straightforwardly for both idler components. In the absence of any external idler inputs or any reflections from the input and output facets of the crystal, the result is that

$$\begin{bmatrix} a_i^{(-)}(z=0) \\ a_i^{(+)}(z=L) \end{bmatrix} = \begin{bmatrix} \tilde{g}_{\mathbf{z}}(\Delta k_-) \\ \tilde{g}_{\mathbf{z}}(\Delta k_+), \end{bmatrix}, \tag{23}$$

where each $a_i^{(\pm)}$ is related to $A_i^{(\pm)}$ according to Eq. (2): $A_i^{(\pm)} = -i(2L/\pi)(\omega_i d_0)(n_i c)^{-1} A_s^* A_p a_i^{(\pm)}$. Equation (23) means that the idler emitted from a QPM grating with perfect antireflection (AR) coatings on the input and output facets is proportional to the normalized transfer function, evaluated at the phase mismatch associated with each direction of idler propagation (either forward or backward). In practice, the inequalities $(\Delta k_+ \sigma_z)^2 \ll 1$ and $(\Delta k_- \sigma_z)^2 \gg 1$ often apply, meaning that the QPM noise pedestal is in the approximately flat region for the forward wave, but is proportional to $1/\Delta k_-^2$ for the backward wave, based on Eq. (9). In $LiNbO_3$ for a DFG process involving a 1.064 μm pump and a 1.55 μm signal with $\sigma_z = 1$ μm, $\Delta k_- \sigma_z \approx 7.9$, while $\Delta k_+ \sigma_z \approx 0.2$.

When using AR-coated samples, Eq. (23) could, for example, be used to determine the feedback into the pump laser(s) as a result of RDC errors. However, for the remainder of this paper, we focus on the much stronger, copropagating components corresponding to $\tilde{g}(\Delta k_+)$.

3. RDC ERRORS: EXAMPLES

In order to illustrate the mean properties of QPM gratings with RDC errors determined in Subsection 2.B, in this section we evaluate the spectrum of some example uniform (periodic) and chirped (aperiodic) QPM gratings.

A. Periodic QPM Gratings

First, we consider in Fig. 2 an example periodic case with RDC errors similar to those typically observed in practice [12]. We assume a grating of length 5 cm with nominal spatial frequency $K_g = 2 \times 10^5$ m^{-1} (period 31.4 μm, comparable to the periods required for 1.064 nm-pumped IR devices), and RDC errors $\sigma_z = 1$ μm. The red curve shows the spectrum $|\tilde{g}_{\mathbf{z}}(k)|^2$ for a particular example of a grating with RDC errors. The black curve shows an ensemble average over 50 such spectra. The blue curve shows the ideal transfer function $|\tilde{g}_{\mathbf{z}_0}|^2$. The inset shows the grating spectrum on a linear scale around first-order QPM. For the spatial frequencies shown, the pedestal is approximately flat. Furthermore, the ideal sinc^2-like functional form shown in the inset is almost unaffected by the RDC errors. QPM gratings with these types of RDC errors were analyzed experimentally and theoretically in [12].

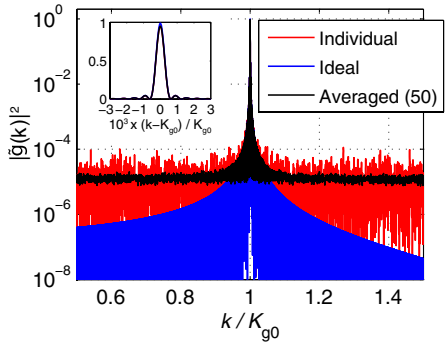

Fig. 2. (Color online) Fourier spectra $|\tilde{g}(k)|^2$ with parameters $\sigma_z = 1$ μm and a 5 cm crystal, and $K_{g0} = 2 \times 10^5$ m^{-1} (≈31.4 μm period). The inset shows $|\tilde{g}(k)|^2$ on a linear scale in the vicinity of first-order QPM; the effects of RDC errors cannot be seen on this linear scale.

To understand Fig. 2 in more detail, Eq. (10) can be rewritten in terms of the grating k-vector $K_g = \pi/\Lambda_D$ (where the nominal grating length $L = N\Lambda_D$). In the vicinity of first-order QPM ($k/K_g \approx 1$), and for RDC errors small enough that $(k\sigma_z)^2 \ll 1$, Eqs. (9) and (10) can be approximated and combined to yield [12]

$$\langle |\tilde{g}(k)|^2 \rangle \approx \frac{1}{N}(1 - e^{-k^2\sigma_z^2}) + e^{-k^2\sigma_z^2} \operatorname{sinc}((k - K_g)L/2)^2. \tag{24}$$

In this equation, the QPM noise pedestal dominates for frequencies sufficiently detuned from the peak that the sinc^2 profile is significantly less than $1/N$ relative to its peak. For the RDC errors and QPM periods typically present in PPLN crystals [12], the prefactor $(1 - \exp(-k^2\sigma_z^2)) \sim 0.05$, thereby leading to a QPM noise pedestal of order $0.05/N$ lower than the peak of $|\tilde{g}_{\mathbf{z}_0}(k)|^2$ (i.e., the peak of the "tuning curve").

Away from first-order QPM, $\tilde{g}_{\mathbf{z}}$ exhibits a number of features in addition to those shown in Fig. 2. To illustrate these features, we next consider in Fig. 3 an example periodic grating with large RDC errors. We assume parameters $L = 5$ cm, $\sigma_z = 3$ μm, and grating k-vector $K_g = 2 \times 10^5$ m^{-1} (QPM period ≈31.4 μm). Spatial frequencies up to grating order 10 are plotted.

The solid blue curve shows the ideal sinc-like transfer function (no RDC errors). The yellow curve shows the spectrum $|\tilde{g}_{\mathbf{z}}(k)|^2$ for a particular example of a grating with domain boundaries $\mathbf{z}$ subject to normally distributed errors with $\sigma_z = 3$ μm. The black curve shows the analytically calculated ensemble average given by Eq. (9). Because of the large

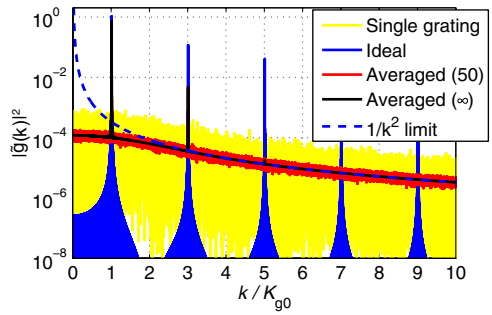

Fig. 3. (Color online) Fourier spectra for a large, 3 μm, mean error in the domain boundaries. The grating is 1 cm long and the grating k-vector is $K_g = 2 \times 10^5$ m^{-1} (QPM period ≈31.4 μm). For the red curve, the spectrum $|\tilde{g}(k)|^2$ was averaged over 50 gratings. The black curve corresponds to the analytical ensemble average from Eq. (9). The dashed blue curve shows a suitably normalized $1/k^2$ profile, which is the asymptotic functional form of the noise pedestal in Eq. (9) for large k.

assumed RDC errors, the higher-order QPM peaks are reduced substantially compared to those of the ideal grating [since $(k\sigma_z)^2$ is large at these spatial frequencies]. Furthermore, since $(k\sigma_z)^2 \not\ll 1$, the pedestal is not flat at high spatial frequencies; the dashed blue curve is proportional to $1/k^2$, and is scaled according to Eq. (8) so as to show the predicted asymptotic behavior of the pedestal for $|k\sigma_z|$ large enough that $\exp(-k^2\sigma_z^2) \ll 1$. Finally, the red curve shows an ensemble average over 50 spectra, showing the same features as the analytically calculated black curve.

B. Chirped QPM Gratings

In periodic QPM gratings, there is a trade-off in the grating length between efficiency and bandwidth; additionally, three-wave nonlinear interactions are subject to backconversion after reaching maximum depletion for one of the waves [36]. With chirped QPM gratings, both of these issues can be avoided simultaneously [37]. The simplest case of a chirped grating corresponds to a linear variation in grating k-vector with position. An example is shown in Fig. 4 (parameters given in the caption). The red curve shows a single spectrum $|\tilde{g}_{\mathbf{z}}|^2$, the black curve shows an ensemble average over 50 such gratings, and the blue curve shows $|\tilde{g}_{\mathbf{z}_0}|^2$.

The ideal Fourier spectrum is broadened and reduced in peak amplitude compared to that of an unchirped grating of the same length. As a result, compared to a periodic grating

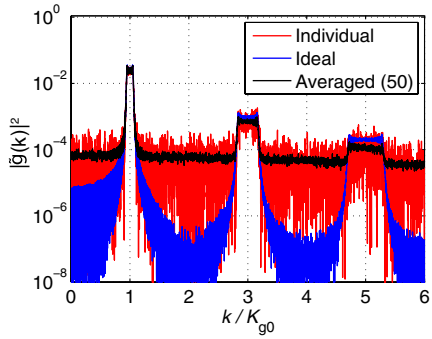

Fig. 4. (Color online) Fourier spectra for an example linearly chirped QPM grating with $\sigma_z = 1$ μm, a chirp rate of $dK_g/dz = 2.5 \times 10^6$ m^{-2}, grating length 1 cm, and mean grating k-vector $K_{g0} = 2 \times 10^5$ m^{-1}.

of the same length and subject to the same RDC errors, the magnitude of the QPM noise pedestal can be considerably closer to the peaks (or "passband") of the ideal transfer function. Additionally, since the k-space bandwidth in a (highly) chirped grating scales with the grating order, higher grating orders are closer still to the pedestal: there is an approximate $1/k^3$ scaling of $|\tilde{g}_{\mathbf{z}_0}(k)|^2$ for ideal chirped QPM gratings. This $1/k^3$ scaling originates from a factor of $1/k^2$ from Eq. (9) and a factor of $1/k$ from the k-space broadening [the $\exp(im\phi(z))$ factor for grating order m in Eq. (12)], together with Parseval's theorem.

This scaling can be seen in Fig. 4 and, as a result, $|\tilde{g}|^2$ is comparable to the QPM noise pedestal in the vicinity of fifth-order QPM: with these 1 μm RDC errors, only the first and third grating orders are above the pedestal. Note, however, that for a fixed first-order QPM conversion efficiency and a fixed spatial-frequency bandwidth of the first Fourier order of the grating, the efficiency of processes phase matched by the noise pedestal is comparable for both chirped and unchirped devices. These conditions apply in practice, given constraints on the conversion efficiency and optical bandwidth, to both chirped and unchirped gratings.

4. APPLICATIONS

In this section, we discuss some specific, representative applications in which the QPM noise pedestal is particularly important.

A. Quantum-State Frequency Translation

Second-order nonlinear interactions can be used to implement frequency conversion of quantum states of light [38,39]. With QPM technology, these quantum frequency conversion (QFC) processes can be performed efficiently with moderate-power continuous-wave (CW) sources. While QFC can in principle be noiseless [38], it has been found that, for pump wavelengths shorter than one of the quantum-state frequencies of interest, the QPM noise pedestal results in an enhancement of nominally phase-mismatched parametric fluorescence [11] and, hence, in the generation of noise photons. When photons generated by parametric fluorescence overlap spectrally with the frequency bands occupied by the signal, the ultrasensitive frequency converter cannot distinguish between the signal and noise photons, which leads to a reduction in the fidelity of the QFC process.

In a 1064 nm pumped single-photon upconversion detector for a 1.55 μm band signal, a noise count rate of approximately 8×10^5 counts/s was observed [9]. Theoretical analysis of the RDC-error-enhanced parametric fluorescence noise for this system [based on Eq. (24)] shows that the observed dark count rate is consistent with $\sigma_z \approx 3.2$ μm [11], which, in turn, is consistent with the observations of lower-than-expected conversion efficiency compared to an ideal QPM grating [9], again predicted by Eq. (24). In [12], RDC errors of $\sigma_z \approx 0.3$ μm were measured directly. A pedestal in SHG conversion efficiency was also observed, and was consistent with Eq. (24) given the measured RDC errors.

RDC error tolerances for achieving a certain conversion efficiency and dark count rate (due to parametric fluorescence) have been derived [11]; these tolerances can be quite stringent for single-photon conversion devices. Spontaneous Raman scattering is another important source of dark counts in

QFC [13]. Both these sources of dark counts can be suppressed significantly by use of a long wave pump [8].

B. Optical Parametric Chirped Pulse Amplification

RDC errors can be an important consideration in OPCPA of mid-IR pulses using MgO:$LiNbO_3$ QPM gratings. With an intense pump pulse and a sufficiently long grating, significant parasitic SHG of the pump can occur due to RDC errors. The intense second harmonic (SH) can in turn lead to TPA and subsequent strong thermal lensing and photorefractive effects, which are detrimental to the OPCPA process. To estimate the severity of this SHG-TPA process, some further analysis beyond that given in Section 2 is required. In this subsection we investigate this process, choosing parameters relevant for OPCPA based on chirped (aperiodic) gratings [21–23].

If diffractive effects are neglected, the two-photon-absorbed SH intensity is given, for small absorptions, by

$$I_{\mathrm{abs}}(z) = \int_0^z \beta_{\mathrm{TPA}} I_{\mathrm{SH}}(z')^2 \mathrm{d}z', \tag{25}$$

where β_{TPA} is the TPA coefficient and I_{SH} is the SH intensity. It is convenient to approximate this integration as a summation over the ensemble-averaged intensities within each domain,

$$\langle I_{\mathrm{abs}} \rangle \approx \left\langle \sum_{q=1}^{N} \Lambda_{D,q} \beta_{\mathrm{TPA}} I_{\mathrm{SH}}(\mathbf{z}[q])^2 \right\rangle \approx \beta_{\mathrm{TPA}} I_{\mathrm{max}}^2 \frac{L}{N} \left\langle \sum_{q=1}^{N} |\tilde{h}_{\mathbf{z}}^{(q)}(k)|^4 \right\rangle, \tag{26}$$

where $\Lambda_{D,q}$ is the length of domain q. In the second form of Eq. (26), we have approximated each $\Lambda_{D,q}$ factor in the sum according to $\Lambda_{D,q} \approx \Lambda_D \equiv L/N$, on the assumption that the total range of QPM periods is relatively small. $\tilde{h}_{\mathbf{z}}^{(q)}(k)$ is the normalized SH amplitude at position $\mathbf{z}[q]$, obtained analogously to Eq. (5) as

$$\tilde{h}_{\mathbf{z}}^{(q)}(k) = \frac{\pi}{kL} \sum_{n=1}^{q} (-1)^n e^{-ik\mathbf{z}[n]}, \tag{27}$$

and hence $\tilde{g}_{\mathbf{z}} = \tilde{h}_{\mathbf{z}}^{(N)}$. The "maximum" SH intensity, denoted I_{max}, is the SH intensity that would be predicted for a perfectly quasi-phase-matched interaction in an ideal periodic grating if pump depletion effects were neglected, and is therefore given by

$$I_{\mathrm{max}} = \frac{n_{\mathrm{SH}} \epsilon_0 c}{2} \left| \frac{2}{\pi} \frac{\omega_1 d_{\mathrm{eff}}}{n_{\mathrm{SH}} c} A_{\mathrm{FH}}^2 L \right|^2. \tag{28}$$

In order to evaluate Eq. (26), we need to find $\langle |\tilde{h}_{\mathbf{z}}^{(m)}|^4 \rangle$. Only slight modifications to Eq. (20) are required to account for the fact that here we are integrating only up to $\mathbf{z}[m]$, not $\mathbf{z}[N] = L$. We therefore find that

$$\begin{aligned} \langle |\tilde{h}_{\mathbf{z}}^{(m)}(k)|^4 \rangle \approx\ & 2m^2 \left(\frac{\pi}{kL}\right)^4 (1 - e^{-(k\sigma_z)^2})^2 \\ & + 4m \left(\frac{\pi}{kL}\right)^2 (1 - e^{-(k\sigma_z)^2}) e^{-(k\sigma_z)^2} |\tilde{h}_{\mathbf{z}_0}^{(m)}(k)|^2 \\ & + e^{-2(k\sigma_z)^2} |\tilde{h}_{\mathbf{z}_0}^{(m)}(k)|^4. \end{aligned} \tag{29}$$

To estimate the SH TPA, we keep only the noise pedestal term in each $\tilde{h}_{\mathbf{z}}^{(m)}$ [the first term in Eq. (29)], under the assumption that the SHG process is highly phase mismatched. By substituting Eqs. (28) and (29) into Eq. (26), summing over the intensity absorbed within each domain, and assuming $N^3 \gg N^2$, the following expression for the total, ensemble-averaged TPA can be obtained:

$$\langle I_{\mathrm{abs}} \rangle \approx \frac{2}{3} \beta_{\mathrm{TPA}} I_{\Lambda}^2 \Lambda_D \left(\frac{L}{\Lambda_D}\right)^3 \left(\frac{\pi\sigma_z}{\Lambda_D}\right)^4 \left(\frac{1 - e^{-k^2\sigma_z^2}}{k^2\sigma_z^2}\right)^2, \tag{30}$$

where Λ_D is the average domain length, and $I_{\Lambda} = I_{\mathrm{max}}(\Lambda_D/L)^2$ is the "maximum" intensity from a single domain of size Λ_D; this latter substitution is made so that Eq. (30) gives the grating-length dependence of $\langle I_{\mathrm{abs}} \rangle$ explicitly. For sufficiently small errors, the final factor in parentheses is equal to 1. Equation (30) indicates that I_{abs} is proportional to σ_z^4, L^3, and I_{FH}^4 (in the context of OPCPA, this FH intensity would correspond to the pump intensity); in comparing different OPCPA devices, it may be worth noting also that $I_{\mathrm{abs}} \propto \sigma_z^4 (I_{\mathrm{FH}} L)^4 / L$.

We next evaluate Eq. (30) with relevant parameters. We assume the following system based on [21–23]: the pump wavelength is 1.064 μm, the material is MgO:$LiNbO_3$, the average domain size is $\Lambda_D = 14.94$ μm (corresponding to OPA for a 3.5 μm idler), and the crystal length is 10 mm. The SHG phase mismatch determines the spatial frequency at which Eq. (30) should be evaluated, and hence $k = 9.317\ \mathrm{m}^{-1}$. We assume RDC errors such that $\sigma_z = 1$ μm [11]. The TPA coefficient of $LiNbO_3$ at 532 nm ($\lambda_p/2$) is $\beta_{\mathrm{TPA}} = 0.38$ cm/W [40], the effective nonlinear coefficient for 1064 nm SHG involving the d_{33} tensor element is $d_{\mathrm{eff}} = 25.2$ pm/V [41], and the dispersion relation is given in [42]. For a first calculation, we assume a CW pump with an intensity of 10 GW/cm^2. With these parameters, we find from Eq. (30) that $\langle I_{\mathrm{abs}} \rangle \approx 2.865$ GW/cm^2 (a remarkably large fraction of the pump).

To estimate the thermal load in the presence of a pulsed pump beam, the SH absorption must be integrated over both space and time. As in Subsection 2.C, a general procedure for such a calculation can be obtained by use of the transfer function approach of [31] (for DFG) and [43] (for SHG). In the case of SHG, provided that GVD of the FH can be neglected, the SH is driven in the frequency domain by the FT of the square of the FH envelope, $\mathcal{F}[A_{\mathrm{FH}}(t)^2]$. Here, we can assume a pump of long enough duration that group velocity mismatch and dispersive effects are negligible, and hence the ensemble-averaged total absorbed energy at the SH is obtained by integrating the local absorbed intensity over space and time,

$$\langle U_{\mathrm{abs}} \rangle = \langle I_{\mathrm{abs}}^{(\mathrm{pk})} \rangle \iiint \bar{I}_{\mathrm{FH}}^4(x, y, t) \mathrm{d}x\mathrm{d}y\mathrm{d}t, \tag{31}$$

where $\bar{I}_{\mathrm{FH}} \equiv I_{\mathrm{FH}}/I_{\mathrm{pk}}$ denotes the normalized FH intensity (maximum equal to 1) and $I_{\mathrm{abs}}^{(\mathrm{pk})}$ denotes the absorbed intensity at the peak of the pulse (intensity I_{pk}). For Gaussian pulses in space and time ($1/e^2$ radius w, FWHM duration τ), the integral in Eq. (31) is given by

$$\iiint \bar{I}_1^4(x, y, t) \mathrm{d}x\mathrm{d}y\mathrm{d}t = \left(\frac{\pi}{8}\right)^{3/2} \frac{w^2 \tau}{\sqrt{2\ln(2)}}. \tag{32}$$

For the example considered above, $\langle I_{\rm abs}^{\rm (pk)}\rangle = 2.865$ GW/cm^2. If we assume a Gaussian pump beam with a FWHM duration of 12 ps and an energy of 300 μJ (corresponding to a beam radius of 387 μm for a peak intensity of 10 GW/cm^2), Eq. (31) implies an ensemble-averaged absorbed energy of 7.18 μJ. At a repetition rate of 100 kHz (30 W pump power), this implies a thermal load of 718 mW, which is very large. Thus, SHG followed by TPA can lead to a significant thermal load on the crystal. With RDC errors of $\sigma_z = 0.5$ μm instead of 1 μm, the predicted thermal load is reduced by almost an order of magnitude, to 81 mW. Sufficient care should therefore be taken in fabricating such QPM devices to obtain submicrometer RDC errors. Note also that, with half the peak intensity (5 GW/cm^2), the thermal load is reduced by a further factor of 16, to 5 mW.

C. Optical Parametric Oscillators: Nonlinear Loss

OPOs enable the generation of widely tunable and high power coherent light across the visible and infrared spectral regions [44–50]. RDC errors may play an important role in OPOs, particularly when there are high resonating intensities. In the presence of the nominal pump, signal, and idler waves (ω_p, ω_s, and ω_i, respectively) components of the nonlinear polarization are also generated at other, related frequencies, such as the SH frequencies $2\omega_j$. The most intense wave in a low-loss OPO not close to threshold is typically the resonant signal. SHG involving this wave constitutes a nonlinear loss mechanism, which for certain cases, in particular for pulsed interactions, could be significant.

Consider first a CW singly resonant OPO (SRO) case, assuming that the nonlinear losses are small and perturbative. The steady-state signal intensity, and hence the pump depletion, is determined by the number of times the pump intensity is above oscillation threshold pump intensity [18,51]; we denote this number as N_p (to distinguish between this quantity and the number of domains in the grating, N). For a low-loss cavity, the amplitude of the signal is given by the implicit relation

$$\mathrm{sinc}^2(\Gamma_s) = N_p^{-1}, \tag{33}$$

where the pump depletion factor Γ_s is given by

$$\Gamma_s^2 = \frac{\omega_i\omega_p(2d_0/\pi)^2|A_s|^2L^2}{n_in_pc^2}. \tag{34}$$

Optimal pump depletion for the SRO occurs at $N_p = (\pi/2)^2$; at this value, $\Gamma_s = \pi/2$. The SH field can be determined in the same way the idler was determined in Section 2, by substituting the value of $|A_s|$ resulting from Eq. (33) into Eq. (2) (with suitable modifications to the coupled-wave equations for SHG instead of DFG [52]) to find the "maximum" signal SH (for a phase-matched first-order QPM interaction), and then applying Eq. (8) to find the actual SH field in terms of the RDC errors. We also allow for the possibility of different tensor elements for the SHG- and OPO-gain processes ($d_{\rm SHG}$ and $d_{\rm OPO}$, respectively), and denote the signal-SHG phase mismatch as $\Delta k_s = k(2\omega_s) - 2k(\omega_s)$. Taking the ratio of the signal and ensemble-averaged SH intensities, we arrive at the following expression for the nonlinear loss:

$$a_{\rm NL} = \frac{\Gamma_s^2}{N}\left(\frac{\pi\sigma_z}{\Lambda_D}\right)^2\frac{1-e^{-\Delta k_s^2\sigma_z^2}}{\Delta k_s^2\sigma_z^2}\frac{n_in_p}{n_sn_{\rm SH}}\frac{\omega_s^2}{\omega_i\omega_p}\left(\frac{d_{\rm SHG}}{d_{\rm OPO}}\right)^2 \equiv \Gamma_s^2a_0, \tag{35}$$

where we have introduced the loss term a_0 for convenience. We assume pump and signal wavelengths of 1.064 and 1.55 μm, respectively, a MgO:LiNbO$_3$ QPM grating operated at 150°C, $\Lambda_D \approx 15$ μm (for the nominal OPO process), and $\Delta k_s = 3.34\times10^5$ m^{-1} (for the parasitic signal SHG process). Choosing the remaining parameters as $\Gamma_s = \pi/2$, $L = 5$ cm, and $\sigma_z = 1$ μm, and $d_{\rm SHG} = d_{\rm OPO}$, Eq. (35) yields $a_{\rm NL} \approx 4.5\times10^{-3}$%, negligible in comparison to the losses of most CW OPOs (which typically have total cavity losses of order 1% or more [15,48]).

For certain pulsed OPOs, however, the energy lost due to signal SHG may be more significant. An analogous form of Eq. (19) that applies for SHG of a pulsed signal is given by

$$\langle W_{\rm SH}\rangle = \frac{2\epsilon_0\omega_s^2d_0^2L\Lambda_D}{n_{\rm SH}c}\frac{1-e^{-\Delta k_s^2\sigma_z^2}}{\Delta k_s^2\Lambda_D^2}\int|A_s(z=0,t)^2|^2\mathrm{d}t. \tag{36}$$

Assuming a Gaussian resonant signal pulse, the ratio of the SH and signal fluences (and hence the nonlinear loss) can be expressed, after some algebra, as

$$a_{\rm NL} = 2^{-1/2}\Gamma_{s,\rm pk}^2a_0, \tag{37}$$

where $\Gamma_{s,\rm pk}$ is Γ_s defined in Eq. (34), evaluated at the peak intensity of the signal pulse, and a_0 is given implicitly by Eq. (35). Note that, if we also integrate over space assuming nondiffracting Gaussian beams, a total nonlinear loss of $a_{\rm NL} = 2^{-3/2}\Gamma_{s,\rm pk}^2a_0$ is obtained. If the peak intensity is significantly larger than the intensity required to achieve high conversion efficiency in a CW OPO, then there will be an increase in the nonlinear loss. Furthermore, for short-pulse OPOs, the crystal length and, hence, the number of domains N appearing in Eq. (35), may be reduced substantially compared with typical CW OPO designs. If we assume $\Gamma_s = \pi$, $L = 3$ mm, $\sigma_z = 1$ μm, and consider a MgO:LiNbO$_3$ OPO utilizing the d_{31} tensor element for gain but with an e-wave resonant signal [17], then SHG of this signal via the d_{33} tensor element will occur in addition to the desired three-wave mixing process (amplification of the signal by the pump). Assuming values for these tensor elements based on the 1.313 μm SHG measurements in [41], and using the $2^{-3/2}$ prefactor above in calculating $a_{\rm NL}$, a total nonlinear loss of $a_{\rm NL} = 2.1$% is obtained. For a nominally low-loss OPO cavity, this additional loss would be very significant.

Based on the above analysis, we can conclude that, for certain short-pulse OPOs, in particular those with low losses and short crystal lengths, RDC errors can lead to a significant nonlinear loss. Nonlinear losses limit the cavity enhancement that can be achieved, and may also lead to instabilities, a reduction in conversion efficiency, and other detrimental effects (although such effects are beyond the scope of this paper).

We note also that there is another loss, denoted a_L, due to the SFG process involving the signal and pump waves ($\omega_s + \omega_p$). Although a_L can be significantly enhanced by RDC errors, this loss will be of order $a_L \sim a_{\rm NL}a_{\rm total}$, where $a_{\rm total}$ denotes the total cavity losses; this scaling arises by assuming that the signal intensity in an above-threshold OPO is of order $1/a_{\rm total}$ times larger than the pump intensity.

Therefore, loss via signal-pump SFG should be negligible in most cases.

D. Optical Parametric Oscillators: Cascaded Processes

In addition to the signal SHG process discussed above, many other "cascaded" spectral components beyond the desired pump, signal, and idler waves can be generated in OPOs (and other nonlinear devices). For infrared OPOs, some of these cascaded components lie in the visible spectrum and can sometimes serve as a clear indication of parametric oscillation. The amount of power generated at visible wavelengths can be surprisingly high, given that the corresponding mixing processes are (usually) nominally phase mismatched. RDC errors explain how these frequencies can be generated with appreciable powers, particularly for pulsed OPOs.

As an example, consider an SRO. As discussed in Subsection 4.C, in the presence of RDC errors, a relatively intense SH can be generated by the resonant signal. This signal SH can in turn sum with the pump to yield SFG spectral components $\omega = 2\omega_s + \omega_p$; this nominally phase-mismatched SFG process can also be enhanced in the presence of RDC errors. For 1064 nm-pumped OPOs with a resonant wavelength between 1.3 and 4 μm, $\omega = 2\omega_s + \omega_p$ lies in the visible spectrum. Note that, for short-wave-resonant SROs, $\omega_s + \omega_p$ also lies in the visible and can be expected to be more efficient than the $2\omega_s + \omega_p$ spectral component. Here we consider this $2\omega_s + \omega_p$ component for several reasons: (1) it will be visible in almost any 1064 nm-pumped OPO, (2) it involves two simultaneous processes, both of which will typically be dominated by the QPM noise pedestal, and is therefore a good example to illustrate an extension of the mathematical approach of Section 2, and (3) for typical OPO parameters, this wave can actually have a small but nonnegligible power that is several orders of magnitude above the power that would be predicted in the absence of RDC errors.

To estimate the intensity of this spectral component, similar integrals to those discussed in Subsection 4.B can be performed. The equations that determine the SFG process are given by

$$\frac{dA_{\mathrm{SH}}}{dz} = -i\frac{\omega_s d(z)}{n_{\mathrm{SH}}c}A_s^2 e^{i\Delta k_s z}, \tag{38a}$$

$$\frac{dA_{\mathrm{SF}}}{dz} = -i\frac{\omega_{\mathrm{SF}} d(z)}{n_{\mathrm{SF}}c}A_p A_{\mathrm{SH}} e^{i\Delta k_{\mathrm{SFG}} z}, \tag{38b}$$

where A_p and A_s are determined by the steady-state OPO solutions. For simplicity, we assume that both A_p and A_s are z-independent (pump depletion is neglected for the purposes of calculating the SFG process).

The sum frequency (SF) is driven by the product $A_{\mathrm{SH}}(z)A_p$. Assuming A_s and A_p are known, A_{SH} can be calculated first via Eq. (38a) and substituted into Eq. (38b) to calculate A_{SF}. $|A_{\mathrm{SF}}|^2$ therefore contains many terms, which must be ensemble averaged separately, as in previous subsections. These calculations yield, after some algebra, an ensemble-averaged normalized SFG intensity given by

$$\langle |a_{\mathrm{SF}}|^2 \rangle \approx \frac{1}{N^2}\left(\frac{2\pi^2}{\Delta k_{\mathrm{SFG}}\Delta k_s \Lambda_D^2}\right)^2 \times \left[1 + e^{-(\Delta k_{\mathrm{SFG}}^2 + \Delta k_s^2)\sigma_z^2} - e^{-\Delta k_s^2 \sigma_z^2} - e^{-\Delta k_{\mathrm{SFG}}^2 \sigma_z^2}\right], \tag{39}$$

where $\Delta k_{\mathrm{SFG}} = k(\omega_p + 2\omega_s) - k(2\omega_s) - k(\omega_p)$ (and $\Delta k_s = k(2\omega_s) - 2k(\omega_s)$). a_{SF} is normalized to the value that would be obtained if both the SFG and signal SHG processes satisfied first-order QPM in an ideal grating and pump depletion effects are neglected, and hence

$$A_{\mathrm{SH}} = -\frac{2\omega_{\mathrm{SF}}\omega_s d_0^2 L^2}{\pi^2 n_{\mathrm{SH}} n_{\mathrm{SF}} c^2} A_p(0) A_s(0)^2 a_{\mathrm{SF}}. \tag{40}$$

With Eq. (40), the ensemble-averaged SF intensity can be expressed as

$$\frac{\langle I_{\mathrm{SF}} \rangle}{I_p} = \frac{n_i^2 n_p}{n_{\mathrm{SH}} n_{\mathrm{SF}}}\left(\frac{\omega_s \omega_{\mathrm{SF}}}{\omega_i \omega_p}\right)^2 \Gamma_s^4 \bar{I}_s^2 |a_{\mathrm{SF}}|^2, \tag{41}$$

where Γ_s is defined in Eq. (34) and $\bar{I}_s$ is the signal intensity normalized to its peak.

The SF intensity may be integrated over space to yield an average power. Consider a MgO:$LiNbO_3$ with crystal length 5 cm, QPM period ≈30 μm, pump and signal wavelengths of 1064 and 1550 nm, respectively, spot sizes of 70 μm, pump power of 10 W, and resonant signal power of 200 W. If diffraction and pump depletion effects are neglected for simplicity and RDC errors with $\sigma_z = 1$ μm are assumed, the corresponding power $P_{\mathrm{SF}} \approx 10$ μW. This is a relatively high power for a CW process involving two cascaded processes, both of which are nominally highly phase mismatched; in the absence of RDC errors and far from phase matching for both processes, the generated power would be several orders of magnitude less.

As in Subsections 4.B and 4.C, the conversion efficiency can be substantially increased for pulsed interactions, and can be estimated from Eq. (41) provided that group velocity mismatch effects can be neglected. From the Γ_s^4 dependence of $\langle I_{\mathrm{SF}} \rangle$, any increase in $\Gamma_{s,\mathrm{pk}}$ beyond $\pi/2$ for pulsed OPOs will rapidly increase the cascaded SFG efficiency.

E. Supercontinuum Generation

In supercontinuum generation [24–27], very high intensities are involved over substantial propagation lengths. As a result, RDC errors can lead to the efficient generation of sum-frequency components (2ω, 3ω, 4ω, and so on, for optical frequency ω). Depending on the particular configuration, these interactions can be viewed as useful (generating carrier envelope offset frequency signals) or as parasitic (removing energy from the FH part of the pulse and thereby reducing the rate of self-phase-modulation responsible for the continuum generation). However, the assumptions made in Subsection 2.C to model pulsed interactions do not apply (since the FH envelope changes substantially). In principle, the various nonlinear processes can be solved fully numerically with no approximations on $d(z)$. However, numerical methods typically assume a smooth grating spatial profile, with only a finite number of QPM orders. In Appendix A, we discuss how RDC errors can be sensibly incorporated into the "Fourier-filtered" propagation schemes used for pulsed interactions, by suitable perturbations of the grating phase profile $\phi(z)$ appearing in Eq. (11). The procedure we discuss should allow the parasitic processes of the types discussed in this section to be (approximately) accounted for when modeling highly nonlinear QPM devices.

5. CONCLUSIONS

In this paper, we investigated the statistical properties of QPM gratings with normally distributed errors in the boundary positions. While the use of lithographic fabrication techniques ensures the long-range order of the grating (thereby preventing QPM period errors), local fluctuations in the boundary positions are still possible. Based on Eq. (9), the resulting ensemble-averaged square-magnitude of the spatial FT of the grating, $\langle|\tilde{g}_{\mathbf{z}}(k)|^2\rangle$, can be described by the FT of the ideal grating structure with an exponential amplitude reduction factor corresponding to the variance of the domain boundary positions, plus a spatial-frequency pedestal whose mean and variance are approximately flat for small spatial frequencies k. This pedestal can enhance the conversion efficiency of nominally phase-mismatched processes.

For certain pulsed interactions, a transfer function approach can be applied, yielding a generated output optical spectrum that is proportional to the spatial-frequency spectrum of the QPM grating, with a mapping $\Delta k(\omega)$ between spatial and optical frequencies determined by the phase mismatch. For more complicated pulsed interactions, RDC errors can be incorporated into numerical simulations by perturbing the grating phase function. In addition to the effects on forward-propagating waves, we also considered the case of backward-generating waves in random QPM gratings. When reflections can be neglected, the normalized backward-generated wave has the same form as the forward wave, but evaluated at the spatial frequency associated with backward phasematching, $\Delta k_- = k_p - k_s + k_i$.

RDC errors can play an important role in a number of applications utilizing QPM gratings. We considered several example device configurations, including QFC, OPCPA, and OPOs. For systems involving high intensities (where RDC errors can lead to high conversion efficiency of parasitic processes), very low intensities (where only a small RDC-error-induced enhancement in parasitic nonlinear processes can scatter too much light into wavelength ranges of interest), and low-loss cavities (where RDC-enhanced nonlinear loss mechanisms limit the achievable cavity enhancement), RDC errors can be a critical consideration. For some applications, RDC-related parasitic processes can be suppressed by system design, while, for other applications, improvements in QPM fabrication are required. Our analysis allows RDC errors and their effects to be understood analytically and modeled numerically, and should therefore be of use in a wide range of applications.

APPENDIX A: RDC ERRORS IN PULSED SYSTEMS

As discussed in Section 4, RDC errors can be particularly important in pulsed systems, where the intensities can be much higher than in CW systems. When the two input pulses for a SFG or DFG process experience negligible depletion and have long enough durations that group velocity walk-off and GVD effects between those two pulses can be neglected, the analysis of Subsection 2.C applies, and the generated field can be expressed in terms of $\tilde{g}_{\mathbf{z}}(\Delta k(\omega))$. However, often depletion and dispersion effects cannot be approximated in this way. In these situations, equations governing the nonlinear interaction must often be solved numerically.

One way to solve these equations is to propagate the electric field through each successive QPM domain individually, accounting for the discrete reversals in the sign of $d(z)$. However, this layer-by-layer approach differs significantly from the numerical methods often used to model pulsed QPM interactions, in which the grating is first expanded in a (local) Fourier series given in Eq. (11), and only the dominant (slowly varying, strongly interacting) terms in the series are retained [26,53].

An alternative way to describe RDC errors mathematically is by a perturbation of the grating phase $\phi(z)$ appearing in Eq. (11), since a change in this phase corresponds to a shift in the domain boundary positions. For a given nonideal QPM structure, there are an infinite number of possible $\phi(z)$ profiles for which Eq. (11) is satisfied. Of these profiles, we would (ideally) choose the one(s) for which $\exp(i\phi(z))$ has the narrowest spatial-frequency bandwidth, so that the relevant properties and statistics of the grating can be described by a small number of harmonic terms in Eq. (11). Rather than select this ideal but unknown choice for a given grating, here we discuss heuristic choices of $\phi(z)$ that maintain the important properties of the QPM noise pedestal.

To analyze phase profiles $\phi(z)$ with random perturbations, we define $\phi_0(z)$ to be the phase profile of the ideal structure, such that the random phase perturbation is given by

$$\delta\phi(z) \equiv \phi(z) - \phi_0(z). \tag{A1}$$

Each time $\phi(z)$ passes through $\pi/2$ or $3\pi/2$ corresponds to a reversal in the sign of $d(z)$. To avoid artificially introducing extra domains via $\delta\phi$, $\phi(z)$ should be increasing, i.e., $d\phi/dz > 0$. Although this assumption could be violated for large enough $\delta\phi(z)$, one way to maintain the monotonicity of $\phi(z)$ (with high probability) is by limiting the magnitude and rate of variation of $\delta\phi(z)$. We note that a somewhat similar issue applies when assuming normally distributed discrete RDC errors defined by $\delta z_n \equiv \mathbf{z}[n] - \mathbf{z}_0[n]$ when calculating $\tilde{g}_{\mathbf{z}}(k)$, as in Section 2: with normally distributed errors, there is a finite probability that $|\delta z_n| > \Lambda_D$ (which would lead to unphysical situations, such as domains with negative length). When dealing with large RDC errors, other statistical assumptions could be made in order to avoid these types of issues.

The shift δz_n in domain boundary n due to RDC errors is given, implicitly, by $\phi(z_{n0} + \delta z_n) - \phi_0(z_{n0}) = 0$. This condition can be re-written as

$$\delta\phi(z_{n0} + \delta z_n) = -(\phi_0(z_{n0} + \delta z_n) - \phi_0(z_{n0})) \approx -K_g(z)\delta z_n, \tag{A2}$$

where the latter relation assumes a constant or slowly varying grating k-vector $K_g(z)$, where $K_g(z) \equiv d\phi_0/dz$. The phase profile should share (approximately) the statistical properties of δz_n; at a fixed z, $\delta\phi(z)$ should thus be normally distributed, and $\delta\phi(z)$ should be negligibly correlated with $\delta\phi(z + \delta x)$ for $|\delta x| > \pi K_g(z)^{-1}$ (to ensure independent domain boundary errors).

Phase profiles with the these properties can be constructed with a Gaussian filter of white noise. Consider a filter with form $h(z) \propto \exp(-(z/w)^2)$ with spatial width w. The resulting standard deviation of the phase $\delta\phi(z)$ after filtering is given by

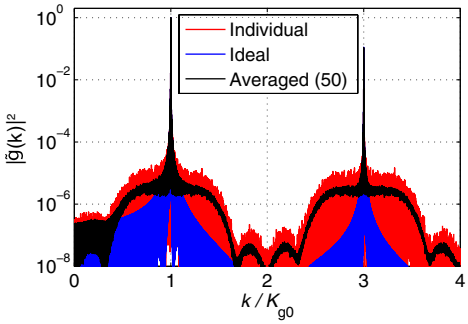

Fig. 5. (Color online) Fourier spectrum arising from domain boundary variations defined by a grating phase perturbation $\delta\phi(z)$ defined by applying a sinc filter to white noise.

$\sigma_{\delta\phi}$. Based on the above considerations, the parameter w must satisfy

$$\sigma_{\delta\phi} \ll K_g w \ll \pi, \tag{A3}$$

where the first condition leads to the monotonicity of $\phi(z)$, and the second condition leads to weak correlations between neighboring domains. Equation (44) can be satisfied only for small RDC errors (i.e., small $\sigma_{\delta\phi}$).

The assumption of normally distributed RDC errors may not always be accurate. Furthermore, the statistical properties of the QPM noise pedestal might sometimes be less important than generating a noise pedestal that has the correct magnitude, extends over the relevant spatial-frequency region (defined by the optical frequencies involved), and can be applied to numerical simulations. In such cases, use of a non-Gaussian filter may be more expeditious. For example, consider a sinc filter with spatial-frequency extent $2K_g$. With $\delta\phi(z)$ determined via convolution with this filter, the Fourier spectrum of each QPM order, $\tilde{g}_z^{(m)}(k)$ [Eq. (12)], extends over a range $2K_g$; summing over all QPM orders, a reasonably flat QPM noise pedestal is produced. This sinc filter yields a noise pedestal at all spatial frequencies after summing over all grating orders, while only requiring a single grating order to be included for any given nonlinear interaction (i.e., the odd-integer value of m that minimizes $|mK_g - \Delta k_{\text{opt}}|$, where Δk_{opt} represents the phase mismatch of the process being modeled).

When a narrow spectral region of the QPM noise pedestal is of interest, a corresponding narrower bandwidth spatial filter for $\phi(z)$ might be used; this case is illustrated in Fig. 5. Although the $\delta\phi(z)$ corresponding to this approximately band-limited noise power spectrum violates the assumed statistical independence of the QPM domains, the reduction in required spatial resolution compared to the Gaussian filter is substantial. In general, provided that a smooth and continuous $\phi(z)$ can be specified for any individual numerical simulation, useful descriptions of RDC errors can be incorporated efficiently and straightforwardly into standard numerical models of pulsed nonlinear interactions in QPM media.

ACKNOWLEDGMENTS

This research was supported by the U.S. Air Force Office of Scientific Research (AFOSR) under grants FA9550-09-1-0233 and FA9550-05-1-0180.

REFERENCES

1. S. Zhu, Y. Zhu, and N. Ming, "Quasi-phase-matched third-harmonic generation in a quasi-periodic optical superlattice," Science **278**, 843–846 (1997).
2. K. Fradkin-Kashi and A. Arie, "Multiple-wavelength quasi-phase-matched nonlinear interactions," IEEE J. Quantum Electron. **35**, 1649–1656 (1999).
3. K. Fradkin-Kashi, A. Arie, P. Urenski, and G. Rosenman, "Multiple nonlinear optical interactions with arbitrary wave vector differences," Phys. Rev. Lett. **88**, 023903 (2001).
4. M. Baudrier-Raybaut, R. Haidar, P. Kupecek, P. Lemasson, and E. Rosencher, "Random quasi-phase-matching in bulk polycrystalline isotropic nonlinear materials," Nature **432**, 374–376 (2004).
5. M. Asobe, O. Tadanaga, H. Miyazawa, Y. Nishida, and H. Suzuki, "Multiple quasi-phase-matched device using continuous phase modulation of $\chi^{(2)}$ grating and its application to variable wavelength conversion," IEEE J. Quantum Electron. **41**, 1540–1547 (2005).
6. R. Lifshitz, A. Arie, and A. Bahabad, "Photonic quasicrystals for nonlinear optical frequency conversion," Phys. Rev. Lett. **95**, 133901 (2005).
7. G. Porat, Y. Silberberg, A. Arie, and H. Suchowski, "Two photon frequency conversion," Opt. Express **20**, 3613–3619 (2012).
8. J. S. Pelc, Q. Zhang, C. R. Phillips, L. Yu, Y. Yamamoto, and M. M. Fejer, "Cascaded frequency upconversion for high-speed single-photon detection at 1550 nm," Opt. Lett. **37**, 476–478 (2012).
9. M. A. Albota and F. C. Wong, "Efficient single-photon counting at 1.55 μm by means of frequency upconversion," Opt. Lett. **29**, 1449–1451 (2004).
10. C. Langrock, E. Diamanti, R. V. Roussev, Y. Yamamoto, M. M. Fejer, and H. Takesue, "Highly efficient single-photon detection at communication wavelengths by use of upconversion in reverse-proton-exchanged periodically poled $LiNbO_3$ waveguides," Opt. Lett. **30**, 1725–1727 (2005).
11. J. S. Pelc, C. Langrock, Q. Zhang, and M. M. Fejer, "Influence of domain disorder on parametric noise in quasi-phase-matched quantum frequency converters," Opt. Lett. **35**, 2804–2806 (2010).
12. J. S. Pelc, C. R. Phillips, D. Chang, C. Langrock, and M. M. Fejer, "Efficiency pedestal in quasi-phase-matching devices with random duty-cycle errors," Opt. Lett. **36**, 864–866 (2011).
13. J. S. Pelc, L. Ma, C. R. Phillips, Q. Zhang, C. Langrock, O. Slattery, X. Tang, and M. M. Fejer, "Long-wavelength-pumped upconversion single-photon detector at 1550 nm: performance and noise analysis," Opt. Express **19**, 21445–21456 (2011).
14. J. Kiessling, R. Sowade, I. Breunig, K. Buse, and V. Dierolf, "Cascaded optical parametric oscillations generating tunable terahertz waves in periodically poled lithium niobate crystals," Opt. Express **17**, 87–91 (2009).
15. C. R. Phillips, J. S. Pelc, and M. M. Fejer, "Continuous wave monolithic quasi-phase-matched optical parametric oscillator in periodically poled lithium niobate," Opt. Lett. **36**, 2973–2975 (2011).
16. A. Henderson and R. Stafford, "Spectral broadening and stimulated Raman conversion in a continuous-wave optical parametric oscillator," Opt. Lett. **32**, 1281–1283 (2007).
17. J. E. Schaar, K. L. Vodopyanov, and M. M. Fejer, "Intracavity terahertz-wave generation in a synchronously pumped optical parametric oscillator using quasi-phase-matched GaAs," Opt. Lett. **32**, 1284–1286 (2007).
18. C. R. Phillips and M. M. Fejer, "Stability of the singly resonant optical parametric oscillator," J. Opt. Soc. Am. B **27**, 2687–2699 (2010).
19. D. T. Reid, "Ultra-broadband pulse evolution in optical parametric oscillators," Opt. Express **19**, 17979–17984 (2011).
20. C. R. Phillips and M. M. Fejer, "Adiabatic optical parametric oscillators: steady-state and dynamical behavior," Opt. Express **20**, 2466–2482 (2012).
21. C. Heese, C. R. Phillips, L. Gallmann, M. M. Fejer, and U. Keller, "Ultrabroadband, highly flexible amplifier for ultrashort midinfrared laser pulses based on aperiodically poled Mg:$LiNbO_3$," Opt. Lett. **35**, 2340–2342 (2010).

22. C. Heese, C. R. Phillips, L. Gallmann, M. M. Fejer, and U. Keller, "Role of apodization in optical parametric amplifiers based on aperiodic quasi-phasematching gratings," Opt. Express **20**, 18066–18071 (2012).
23. C. Heese, C. R. Phillips, B. W. Mayer, L. Gallmann, M. M. Fejer, and U. Keller, "75 MW few-cycle mid-infrared pulses from a collinear apodized APPLN-based OPCPA," Opt. Express **20**, 26888–26894 (2012).
24. T. Fuji, J. Rauschenberger, A. Apolonski, V. S. Yakovlev, G. Tempea, T. Udem, C. Gohle, T. W. Haensch, W. Lehnert, M. Scherer, and F. Krausz, "Monolithic carrier-envelope phase-stabilization scheme," Opt. Lett. **30**, 332–334 (2005).
25. C. Langrock, M. M. Fejer, I. Hartl, and M. E. Fermann, "Generation of octave-spanning spectra inside reverse-proton-exchanged periodically poled lithium niobate waveguides," Opt. Lett. **32**, 2478–2480 (2007).
26. C. R. Phillips, C. Langrock, J. S. Pelc, M. M. Fejer, I. Hartl, and M. E. Fermann, "Supercontinuum generation in quasi-phase-matched waveguides," Opt. Express **19**, 18754–18773 (2011).
27. C. R. Phillips, C. Langrock, J. S. Pelc, M. M. Fejer, J. Jiang, M. E. Fermann, and I. Hartl, "Supercontinuum generation in quasi-phase-matched $LiNbO_3$ waveguide pumped by a Tm-doped fiber laser system," Opt. Lett. **36**, 3912–3914 (2011).
28. S. Helmfrid and G. Arvidsson, "Influence of randomly varying domain lengths and nonuniform effective index on second-harmonic generation in quasi-phase-matching waveguides," J. Opt. Soc. Am. B **8**, 797–804 (1991).
29. M. M. Fejer, G. A. Magel, D. H. Jundt, and R. L. Byer, "Quasi-phase-matched second harmonic generation: tuning and tolerances," IEEE J. Quantum Electron. **28**, 2631–2654 (1992).
30. G. Rosenman, K. Garb, A. Skliar, M. Oron, D. Eger, and M. Katz, "Domain broadening in quasi-phase-matched nonlinear optical devices," Appl. Phys. Lett. **73**, 865–867 (1998).
31. G. Imeshev, M. M. Fejer, A. Galvanauskas, and D. Harter, "Pulse shaping by difference-frequency mixing with quasi-phase-matching gratings," J. Opt. Soc. Am. B **18**, 534–539 (2001).
32. R. W. Boyd, *Nonlinear Optics*, 3rd ed (Academic, 2008).
33. M. Born, E. Wolf, and A. B. Bhatia, *Principles of Optics: Electromagnetic Theory of Propagation, Interference and Diffraction of Light* (Cambridge University, 1999).
34. M. Charbonneau-Lefort, B. Afeyan, and M. M. Fejer, "Optical parametric amplifiers using chirped quasi-phase-matching gratings I: practical design formulas," J. Opt. Soc. Am. B **25**, 463–480 (2008).
35. D. S. Chemla and J. Zyss, *Nonlinear Optical Properties of Organic Molecules and Crystals* (Academic, 1987).
36. J. A. Armstrong, N. Bloembergen, J. Ducuing, and P. S. Pershan, "Interactions between light waves in a nonlinear dielectric," Phys. Rev. **127**, 1918–1939 (1962).
37. C. R. Phillips and M. M. Fejer, "Efficiency and phase of optical parametric amplification in chirped quasi-phase-matched gratings," Opt. Lett. **35**, 3093–3095 (2010).
38. P. Kumar, "Quantum frequency conversion," Opt. Lett. **15**, 1476–1478 (1990).
39. S. Tanzilli, W. Tittel, M. Halder, O. Alibart, P. Baldi, N. Gisin, and H. Zbinden, "A photonic quantum information interface," Nature **437**, 116–120 (2005).
40. R. DeSalvo, A. Said, D. Hagan, E. Van Stryland, and M. Sheik-Bahae, "Infrared to ultraviolet measurements of two-photon absorption and n_2 in wide bandgap solids," IEEE J. Quantum Electron. **32**, 1324–1333 (1996).
41. I. Shoji, T. Kondo, A. Kitamoto, M. Shirane, and R. Ito, "Absolute scale of second-order nonlinear-optical coefficients," J. Opt. Soc. Am. B **14**, 2268–2294 (1997).
42. O. Gayer, Z. Sacks, E. Galun, and A. Arie, "Temperature and wavelength dependent refractive index equations for MgO-doped congruent and stoichiometric $LiNbO_3$," Appl. Phys. B **91**, 343–348 (2008).
43. G. Imeshev, A. Galvanauskas, D. Harter, M. A. Arbore, M. Proctor, and M. M. Fejer, "Engineerable femtosecond pulse shaping by second-harmonic generation with Fourier synthetic quasi-phase-matching gratings," Opt. Lett. **23**, 864–866 (1998).
44. R. G. Smith, J. E. Geusic, H. J. Levinstein, J. J. Rubin, S. Singh, and L. G. Van Uitert, "Continuous optical parametric oscillation in $Ba_2NaNb_5O_{15}$," Appl. Phys. Lett. **12**, 308–310 (1968).
45. R. L. Byer, M. K. Oshman, J. F. Young, and S. E. Harris, "Visible CW parametric oscillator," Appl. Phys. Lett. **13**, 109 (1968).
46. S. T. Yang, R. C. Eckardt, and R. L. Byer, "Continuous-wave singly resonant optical parametric oscillator pumped by a single-frequency resonantly doubled Nd:YAG laser," Opt. Lett. **18**, 971–973 (1993).
47. L. E. Myers and W. R. Bosenberg, "Periodically poled lithium niobate and quasi-phase-matched optical parametric oscillators," IEEE J. Quantum Electron. **33**, 1663–1672 (1997).
48. A. Henderson and R. Stafford, "Low threshold, singly-resonant CW OPO pumped by an all-fiber pump source," Opt. Express **14**, 767–772 (2006).
49. M. J. McCarthy and D. C. Hanna, "All-solid-state synchronously pumped optical parametric oscillator," J. Opt. Soc. Am. B **10**, 2180–2190 (1993).
50. G. J. Hall, M. Ebrahimzadeh, A. Robertson, G. P. A. Malcolm, and A. I. Ferguson, "Synchronously pumped optical parametric oscillators using all-solid-state pump lasers," J. Opt. Soc. Am. B **10**, 2168–2179 (1993).
51. S. T. Yang, R. C. Eckardt, and R. L. Byer, "Power and spectral characteristics of continuous-wave parametric oscillators: the doubly to singly resonant transition," J. Opt. Soc. Am. B **10**, 1684–1695 (1993).
52. R. Eckardt and J. Reintjes, "Phase matching limitations of high efficiency second harmonic generation," IEEE J. Quantum Electron. **20**, 1178–1187 (1984).
53. M. Conforti, F. Baronio, C. De Angelis, M. Marangoni, and G. Cerullo, "Theory and experiments on multistep parametric processes in nonlinear optics," J. Opt. Soc. Am. B **28**, 892–895 (2011).